

Boosting strong metal-support interactions between Ru and sodium titanate nanowire for hydrogenolysis of polyolefins under mild conditions

Xueping Zhang^a, Quan Gan^a, Peng Zhou^b, Zhong Chen^c, Zehui Zhang^{b,*}, Guo-Ping Lu^{a,*}

^a School of Chemistry and Chemical Engineering, Nanjing University of Science and Technology, Nanjing 210094, China

^b School of Chemistry and Materials Science, South-Central Minzu University, Wuhan 430074, China

^c School of Materials Science & Engineering, Nanyang Technological University, 50 Nanyang Avenue, 639798, Singapore



ARTICLE INFO

Keywords:

Hydrogenolysis of polyolefins
Liquid alkanes
Strong metal-support interactions
Ru nanoparticles
Sodium titanate nanowire

ABSTRACT

Catalytic hydrogenolysis provides promising opportunities for the chemical recycling of polyolefins. In this study, we have successfully developed a novel catalyst consisting of ruthenium (Ru) nanoparticles supported on sodium titanate nanowires (Ru@NTO-NH) for the hydrogenolysis of low-density polyethylene (LDPE) into high-value long-chain alkanes under mild reaction conditions (180 °C, 1–2 MPa H₂), achieving yields of up to 91%. Control experiments and thorough characterizations have elucidated that the exceptional catalytic performance of Ru@NTO-NH in the hydrogenolysis of polyolefins can be attributed to strong metal-support interactions (SMSI). NTO-NH exhibits stronger SMSI with Ru species than TiO₂, leading to the formation of smaller Ru nanoparticles that are more positively charged and NaTiO_x-overlayered. This unique configuration facilitates the adsorption and activation of H₂ as well as the desorption of alkanes, thereby enhancing catalytic efficiency and selectivity towards liquid alkanes. Moreover, the Ru@NTO-NH catalyst demonstrates remarkable stability throughout recycling experiments (10 runs). Notably, apart from LDPE, high-density polyethylene (HDPE) and polypropylene (PP) can also be effectively converted into liquid alkanes through hydrogenolysis using this catalyst.

1. Introduction

Polyolefin is the most widely used type of plastics, accounting for approximately 57% of the total plastic production worldwide. It has been found that polyolefin plastics can persist in the soil environment for over 400 years [1]. Therefore, the degradation of polyolefins is a critical aspect of plastic control [2]. Currently, more than 70% of plastic waste is disposed of in landfills, nature, or incinerated, which pose a significant threat to the environment [3]. Consequently, the development of efficient, cost-effective, and environmentally friendly strategies for degrading waste polyolefin plastics has become a major research focus in the field of plastic management [4]. Chemical recycling offers considerable advantages over landfilling, incineration, and biodegradation methods, as it enables the conversion of waste plastics into value-added chemicals within a short timeframe [5]. In the context of polyolefins, chemical degradation and recovery technologies primarily involve two main approaches: pyrolysis and catalytic hydrogenolysis. High temperature pyrolysis can depolymerize polyolefins by breaking strong C-C bonds in them, producing small molecules [6]. However,

these processes are energy intensive and offer low control over product selectivity [7]. Alternatively, selective depolymerization of polyolefins into liquid alkanes with target molecular weight range by catalytic hydrogenolysis of C-C bonds has been popular research recently [8]. The development of efficient and sustainable methods for the degradation of polyolefin plastics is crucial for effective plastic management. Chemical recycling, particularly through catalytic hydrogenolysis, holds promise for converting waste polyolefins into valuable chemicals, offering an alternative to conventional disposal methods.

Recent reports have shown that noble metal ruthenium nanoparticles deposited on silica, alumina, ceria, niobium, tungsten oxide, zirconia, zeolite or carbon in the presence of H₂ can easily break C-C bonds in the polyolefin backbone via hydrogenolysis and produce low molecular-weight wax or fuel-range hydrocarbons. For example, supported Ru catalysts such as Ru/C [9], Ru/CeO₂ [10], Ru/WZrO_x [11], Ru/TiO₂ [12], displayed good catalytic performance for hydrogenolysis of polyolefin. Although great progress has been made rapidly, the main drawback of Ru-based catalysts is its strong tendency to break terminal C-C bonds, which results in forming low-value methane and other light

* Corresponding authors.

E-mail addresses: zehuizh@mail.ustc.edu.cn (Z. Zhang), glu@njust.edu.cn (G.-P. Lu).

alkanes [9d,10b,13]. In addition, most Ru-catalyzed hydrogenolysis of polyolefins also encounter some issues, such as harsh reaction conditions ($T > 250^\circ\text{C}$, H_2 pressure $> 3 \text{ MPa}$), poor catalyst recovery. Hence, the exploration of high-performance Ru catalysts to achieve selective hydrogenolysis of polyolefin plastics under mild reaction conditions is appealing and significant.

To date, it has been found that the support type has a great influence on the performance of Ru catalysts for hydrogenolysis of polyolefins, but only few reports address this crucial observation [9]. For example, Tomishige's group disclosed that Ru/CeO₂ has better catalytic activity and selectivity than other metal oxide supported Ru catalysts, because the basic property of CeO₂ is beneficial to the dispersion of Ru species [10b]. The Vlachos's group proposed a facile method to regulate the metal support interaction (MSI) in Ru/TiO₂, and demonstrated that the stronger MSI can improve the ability of Ru NPs to adsorb and activate H₂, thereby promote the hydrogenolysis of polyolefins [12b]. The Pérez-Ramírez's team proposed that the TiO₂ crystal phase type is related to the degree of the strong metal-support interaction (SMSI), which ultimately affects PE hydrogenolysis [12c]. It is well known that SMSI has a strong impact on the activity and selectivity of heterogeneous catalysts [14,15]. However, there are a handful of studies on improving the efficiency of polyolefin hydrogenolysis by SMSI modification, mainly focusing on TiO₂-supported Ru-based catalysts [12b,12c]. Thus, the possibility of other supported catalysts with SMSI in polyolefin hydrogenolysis still needs to be further explored.

Herein, a newly developed sodium titanate nanowire supported ruthenium catalyst (Ru@NTO-NH) has been disclosed. LDPE can be selectively converted to high-value long-chain alkanes ($\geq \text{C}6$) at 180°C and 1 MPa H_2 with excellent recovery performance. The catalyst also shows excellent catalytic performance for the hydrolysis of other commonly used polyolefin plastics in life, such as PE plastic bag and PP bottle. Further characterization and experiments suggest that the SMSI between Ru and NTO can be adjustable by controlling the calcination conditions, which plays a significant role in the catalytic performance for polyolefin hydrogenolysis.

2. Experimental sections

2.1. Catalyst preparation

Synthesis of sodium titanate nanowires (NTO) and hydrogen titanate nanowires (HTO): The synthesis approach refers to the preparation process in the literature [16]. In a typical synthesis, 1.2 g of TiO₂ powder was dispersed in 60 mL of NaOH (10 M) solution, stirred continuously until the dispersion was uniform, and then transferred to a 100 mL stainless steel autoclave, which was placed in an oil bath at

slowly dripped to NTO dispersion. At room temperature, stirring for 2 h, then slowly dripping 25 mL NaBH₄ aqueous solution (60 mmol/L) into the mixture, reducing for 2 h. Then the precursor Ru@NTO was obtained by spinning and drying. The precursors were pretreated at 400°C for 2 h in N₂ atmosphere, and then Ru@NTO-N was obtained by natural cooling. Ru@NTO-NH was obtained by vacuum drying after washing and roasting at 450°C for 3 h in 5 vol% H₂/Ar atmosphere. Ru@NTO-H was obtained by direct reduction of the precursor at 450°C for 3 h in Ar/H₂ atmosphere. During the preparation of Ru@NTO-NH, the amount of Ru added was 5 wt%, and the content of Ru in Ru@NTO was about 5.1 wt% measured by ICP-MS (Table S1).

The synthesis of other Ru/supports (TiO₂, WO₃, CeO₂, MgO, γ -Al₂O₃, HTO) catalysts is the same as that of Ru@NTO-NH catalysts except for the replacement of supports. The synthetic procedures of Ru/NTO-NH are the same with that of Ru@NTO-NH, with the exception that the NaBH₄ reduction process is not included in the preparation process.

2.2. Catalytic activity tests

The typical procedure for hydrogenolysis of LDPE on Ru@NTO-NH is as follows, and the activity test is carried out in a 30 mL stainless steel autoclave reactor. LDPE (500 mg) and Ru@NTO-NH (100 mg) were put into stainless steel autoclave reactor, whose interior is a slender cylinder with a small bottom area of about 2 cm². After feeding, the catalyst and LDPE were thoroughly mixed by mechanical grinding, then assemble the stainless-steel autoclave reactor, and adding a small cylindrical rotor. After sealing, the reactor was purged with H₂ for 6 times and pressurized to 1 MPa with H₂, then put into a preheated heating device. The reactor was heated to 180°C at the stirring speed of 600 rpm and reacted for 8 h. The melting point of LDPE is $108\text{--}126^\circ\text{C}$, and the reaction takes place at 180°C , where the raw material also serves as the solvent.

After the end of the reaction, the components in the kettle were cooled and collected for analysis. The liquid phase products are dissolved in dichloromethane, filtered and separated from the solid liquid phase, and the solid phase is dried and weighed (Fig. S1). The dichloromethane in the liquid product was dried and weighed, and the conversion and liquid selectivity were calculated. The quantitative 9,10-dihydroanthracene was added to the liquid phase as the internal standard, which was diluted to a certain concentration with quantitative dichloromethane, and the component selectivity of the liquid product was analyzed by gas chromatography. The maximum carbon number which can be analyzed by GC-FID is 35 due to high boiling point of products, and product distribution was decided as follows: gas (C1-C5), liquid fuel (C6-C21), wax (C22-C35). The conversion and yield were calculated with the formulas shown below:

$$\text{Conversion}[\%] = \left(\frac{\text{Amount of substrate input[g]} - \text{Amount of unreacted substrate[g]}}{\text{Amount of substrate input[g]}} \right) \times 100$$

130°C , stirring for 24 h (the stirring speed affects the morphology of the nanowires, and the stirring speed remains unchanged each time). After the reaction, the autoclave was removed from the oil bath and cooled to room temperature. The product sodium titanate (NTO) was collected by centrifugation, washed 6 times with deionized water, and then air-dried at 80°C to obtain a sodium titanate nanowire material.

HCl aqueous solution (1 M, 10 mL×2) is employed for washing NTO (1 g) twice to exchange Na⁺, followed by deionized water until neutral. The solid obtained through filtration is HTO.

Synthesis of Ru@NTO-X (X = N, H, NH): The catalyst was prepared by impregnation approach. 300 mg NTO was dispersed in 30 mL deionized water, and 25 mL RuCl₃ aqueous solution (6 mmol/L) was

$$\text{Liquid phase yield}[\%] = \frac{\text{Liquid phase product content[g]}}{\text{Amount of substrate added[g]}} \times 100$$

$$\text{Gas yield}[\%] = \text{Conversion}[\%] - \text{Liquid phase yield}[\%]$$

$$\text{Selectivity}[\% - C] = \frac{\text{Amount of each products [mol} - C\text{]}}{\sum \text{Amount of product[mol} - C\text{]}} \times 100$$

$$\text{Yield}[\% - C] = \text{Conversion}[-] \times \text{Selectivity}[-] \times 100$$

The residual solids collected after the reaction is assumed to be unreacted substrates and catalysts, although unreacted substrates could

partially react. The amount of unreacted substrate is estimated according to the following equation: the unreacted substrate (g) = (the residual solid weight (g)) - (the introduced catalytic amount (g)), and the experimental error is within the range of $\pm 10\%$.

2.3. Characterization methods

X-ray diffraction (XRD) analysis was conducted using a Shimadzu X-ray diffractometer (XRD-6000) with Cu K α irradiation. Transmission electron microscopy (TEM) images were captured utilizing a PHILIPS Tecnai 12 microscope operating at 120 kV. High-angle annular dark-field scanning transmission electron microscopy (HAADF-STEM) images at atomic resolution were obtained using a FEI Titan Cubed Themis G2 300 S/TEM equipped with a probe corrector and a monochromator, operating at 200 kV. X-ray photoelectron spectroscopy (XPS) measurements were performed on an ESCALAB 250Xi spectrometer, employing an Al K α X-ray source (1350 eV) and calibrated by referencing the C 1 s peak to 284.80 eV. Inductively coupled plasma mass spectrometry (ICP-MS) analysis was conducted on an Optima 7300 DV instrument. BET surface area and pore size measurements were carried out using N₂ adsorption/desorption isotherms at 77 K, employing a Micromeritics ASAP 2020 instrument. Prior to measurements, the samples were degassed at 150 °C for 12 h. Diffuse reflectance infrared Fourier transform spectroscopy (DRIFT) spectra were recorded using a Bruker Equinox 55 spectrometer. For CO adsorption measurements, the sample underwent in-situ pretreatment with H₂ at 450 °C for 1 h, followed by cooling to 25 °C. The gas flow was then switched to He and maintained at this temperature for 0.5 h before collecting the background spectrum. Subsequently, 5 vol% CO/He was introduced until saturation of CO adsorption was achieved. The system was then purged with He to remove gaseous CO, after which the CO-DRIFT spectrum was collected in Kubelka-Munk mode. Temperature-programmed reduction of H₂ (H₂-TPR) was performed using a Micromeritics AutoChem II 2920 instrument. For H₂-TPR. The sample was subjected to a 1 h pretreatment with Ar at 300 °C, followed by cooling to 100 °C. Subsequently, the sample underwent a 30 min purging step with an inert gas at 100 °C. Finally, a 10 vol% H₂/Ar mixture was introduced into the system, and the temperature was increased from 100 °C to 800 °C using a heating rate of 10 °C/min. For temperature-programmed desorption of H₂ (H₂-TPD) analysis, the sample was pre-reduced in a 60-sccm flow of 5% H₂ mixed with He at 523 K for 1 h. It was then cooled to room temperature and purged with a 60-sccm flow of He gas for at least 1 h to stabilize the baseline of the H₂ mass spectrometry (MS) signal. Subsequently, H₂-TPD measurements were conducted using the same ramping program. The MS signal was calibrated using a MicroGC (990 MicroGC, Agilent) equipped with an MS5A column. The MS signal of He was used as a semi-quantitative internal reference for H₂ adsorption/desorption. Butane-TPD was performed in a quartz tube reactor, and the exhaust gas was

analyzed using an HIDEN HPR20 online mass spectrometer. The experimental procedure was similar to that of H₂-TPD, with the exception that butane vapor was introduced instead of H₂ into the catalyst with Ar flow at room temperature. The temperature was increased from 30 °C to 800 °C at a rate of 10 °C/min, and the MS signal of $m/z = 58$ (butane) was continuously recorded. Raman spectra were acquired on a Horiba HR evolution spectrometer using a 532 nm green laser (5 mW power), $\times 50$ objective, and 1800 g/mm grating. The detector resolution under these conditions is approximately 0.48 cm $^{-1}$ /pixel. O₂ temperature-programmed oxidation (O₂-TPO) was conducted in a 10% O₂/Ar flow, raising the temperature from 30 °C to 800 °C at a rate of 15 °C/min. Electron paramagnetic resonance (EPR) measurements were performed on a Bruker A300 EPR EMX Nano Spectrometer at 77 K.

3. Results and discussion

As shown in Fig. 1, TiO₂ reacts with NaOH to grow NTO by mechanical stirring in a hydrothermal setup [16]. Ru@NTO is prepared by an impregnation-reduction method. The use of NaBH₄ in the impregnation process is for effective adsorption Ru species in the support (Fig. S2). Ru is impregnated on the support of NTO and calcinated under N₂ or H₂ atmosphere to produce Ru@NTO-N and Ru@NTO-H, respectively. The catalyst obtained after both N₂ calcination and H₂ reduction is named Ru@NTO-NH. As a comparison, Ru/TiO₂, Ru/HTO-NH was also prepared with the similar procedures of Ru@NTO-NH.

NTO exhibits a nano hollow wire structure, which is consistent with the literature results (Fig. S3a) [16]. The doping of Ru does not significantly change the morphology of NTO (Fig. 2a). Further calcination increases the crystallinity of NTO (Figs. 2c-e), which is broken into shorter nanowires (Fig. S3a vs S3b). The HAADF-STEM images and EDS mapping results proved that Ru was loaded on NTO in the form of nanoparticles (Fig. S3c and S3d) and the Ru NPs with average size about 1.95 nm are uniform dispersed in Ru@NTO-NH (Fig. 2f). Although Ru NPs are also homogeneously distributed on the surface of polygonal TiO₂ particles, its average particle size is larger than that over Ru@NTO-NH (3.10 nm vs 1.95 nm) (Figs. 2g,h). The formation of small-sized Ru nanoparticles on NTO might be due to the introduction of alkali sites and larger specific surface area [17].

The specific surface area and pore volume of Ru@NTO-NH were 40.7 m²/g and 0.2 cm³/g, respectively, which are higher than those of Ru/TiO₂ (21.6 m²/g and 0.1 cm³/g) (Fig. S4, Table S2). Therefore, NTO with larger specific surface area can provide more area in contact with the reactants than TiO₂ and can expose more active Ru sites. The BET specific surface area of Ru@NTO-NH is smaller than that of Ru@NTO (64.6 m²/g) since high-temperature calcination damages the structure of NTO, causing its aggregation.

XRD characterization of the NTO reveals the presence of several crystalline phases and amorphous components. The main diffraction

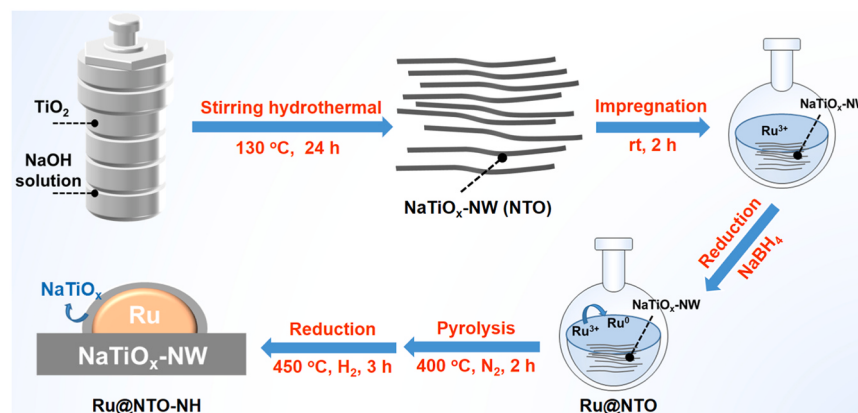


Fig. 1. The synthesis strategy of Ru@NTO-NH.

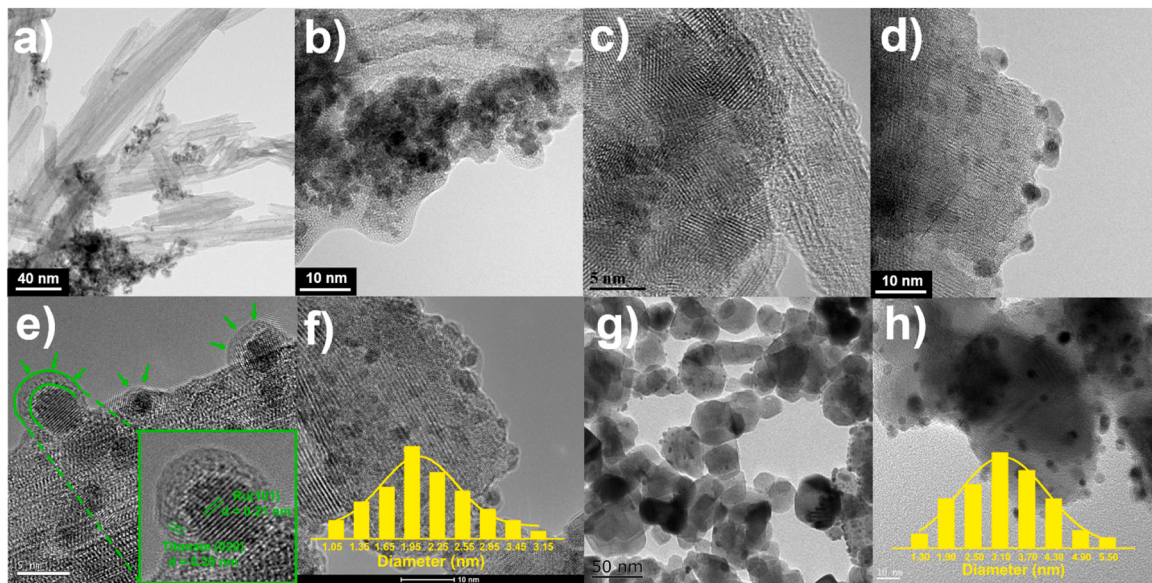


Fig. 2. (a) TEM and (b) HRTEM images of Ru@NTO; HRTEM images of (c) Ru@NTO-N, (d) Ru@NTO-H, (e, f) Ru@NTO-NH; (g) TEM and (h) HRTEM images of Ru/TiO₂. The Ru loading of the above materials is 5 wt%.

peaks can be attributed to the Na₂Ti₃O₇, Na₂Ti₄O₉, Na₂Ti₉O₁₉, and Na₄Ti₅O₁₂ crystalline phases, while the remaining peaks may correspond to amorphous components. The diffraction peaks of Ru species (including Ru and RuO₂) are not detected in both XRD patterns of Ru@NTO-NH and Ru/TiO₂, indicating a high dispersion of Ru material on the support [18] (Fig. S5), which is consistent with the HRTEM results.

The morphology of the catalyst interface was further investigated. The Ru NPs were encapsulated by the NTO-derived NaTiO_x overlayers

with a thickness of ~1.25 nm (Fig. 2e). The crystal plane spacing of 0.21 nm and 0.20 nm was measured and assigned to the (101) plane of metallic Ru and the (020) plane of orthorhombic titanate crystal structure [16a,19]. In addition, the loaded Ru NPs were partially encapsulated by TiO_x overlayers (Fig. 2e). In order to understand the process for the formation of the NaTiO_x overlayers between Ru and NTO, five NTO-supported Ru catalysts prepared by different conditions were detected by HRTEM. It is observed that NaTiO_x also wraps around Ru NPs in the Ru@NTO (Fig. 2b). After N₂ calcination, the crystallinity of

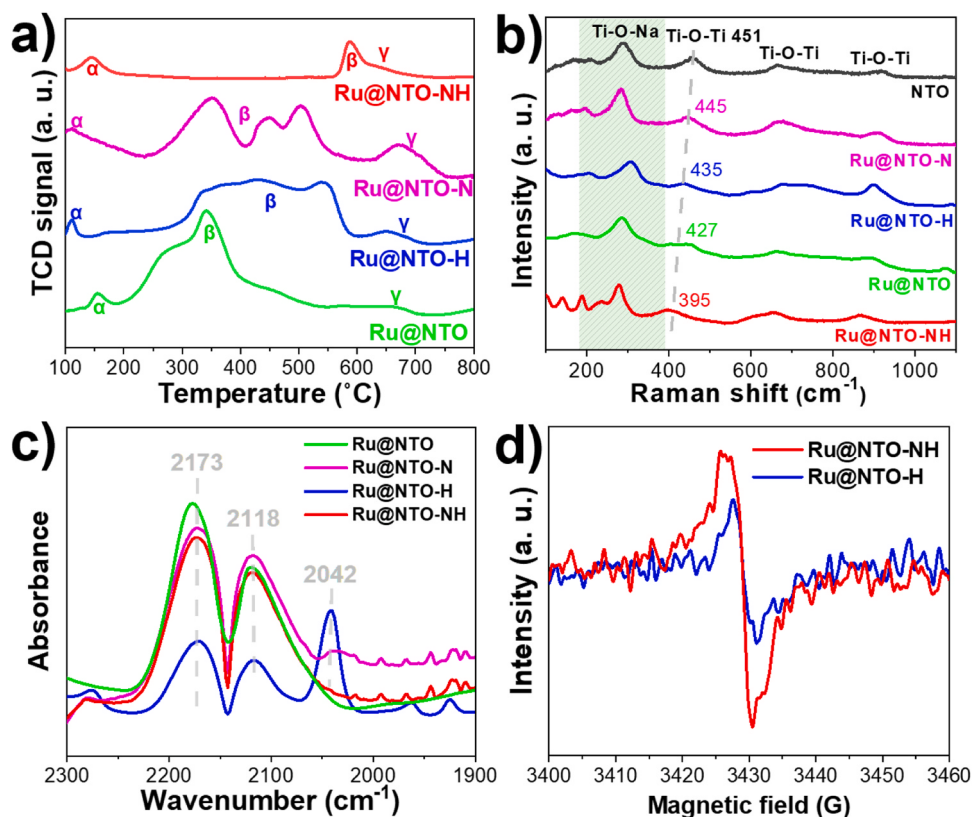


Fig. 3. Spectra of (a) H₂-TPR, (b) Raman, (c) CO-adsorption FT-IR and (d) EPR profiles. The Ru loading of the above materials is 5 wt%.

NTO is improved (Fig. 2c). The distribution of Ru species is poor in both Ru@NTO and Ru@NTO-N catalysts (Fig. S6a and S6b). In contrast to Ru@NTO and Ru@NTO-N catalysts, Ru NPs are more dispersed in Ru@NTO-H and Ru@NTO-NH catalysts containing cladding layers (Figs. 2d,e and S5c), which is attributed to the anchoring of the metal by the NaTiO_x overlayers [20]. Obvious aggregation of Ru particles is observed in the case of Ru/NTO-NH, and there is no overlayer on the Ru particles (Fig. S6d), so the NaBH₄ reduction step is necessary for the formation of SMSI.

In order to clarify the SMSI effect between Ru NPs and NTO, we first analyzed the reducibility of ruthenium metal on the catalyst by temperature-programmed reduction (TPR) analysis. According to H₂ temperature-programmed reduction (TPR) results (Fig. 3a), there are three main reduction features at 100–200 °C (α), 200–600 °C (β) and 600–700 °C (γ). The low-temperature feature peak (α) corresponds to the reduction of surface RuO_x [15a]. The feature peak (β) is mainly attributed to the reduction of Ti⁴⁺ to Ti³⁺ in NTO [20]. The feature peak (γ) belongs to the reduction of Ru species that interacted strongly with the support [21]. The characteristic peaks in the range of 200–600 °C (β) are not only related to Ti³⁺ and the oxygen vacancy [22], but also to the specific surface area and material structure, so it is unable to determine the number of Ti³⁺ and oxygen vacancies in these catalysts based on H₂-TPR results. Compared to Ru@NTO-NH, the lower temperature range and the wider feature peaks (β) of Ru@NTO, Ru@NTO-N and Ru@NTO-H can be attributed to their loose crystal structure and the presence of Na⁺, which makes NTO easier to be reduced [15a,20].

The Raman spectra also prove the existence of SMSI (Fig. 3b), the characteristic peaks below 400 cm⁻¹ can be attributed to surface Ti-O-Na vibration, and adsorption band above 400 cm⁻¹ can be interpreted as Ti-O-Ti crystal phonons [23]. The Ti-O-Ti characteristic signals red-shifted in these samples compared with NTO, indicating that (1) there are SMSI between NTO and Ru NPs; (2) the SMSI may be enhanced by N₂ calcination and H₂ reduction; (3) the SMSI become stronger in order of Ru@NTO-NH > Ru@NTO > Ru@NTO-H > Ru@NTO-N [24].

These NTO-supported Ru catalysts were further characterized by CO adsorption FT-IR and XPS to confirm the SMSI effects. The CO adsorbed on Ru@NTO-H exhibits obvious bands at 2173, 2118, and 2042 cm⁻¹ (Fig. 3c), which are attributed to the CO adsorption on NTO [12b], partially oxidized Ruⁿ⁺ and Ru⁰, respectively [25]. According to HRTEM and XPS results (Figs. 2d and 4a), there are more Ru⁰ sites exposed on the surface of Ru@NTO-H, so the CO adsorption peak at 2042 cm⁻¹ is more significant. There is no obvious CO adsorption signal at 2042 cm⁻¹ in the cases of Ru@NTO, Ru@NTO-N and Ru@NTO-NH owing to the existence of denser NaTiO_x overlayer (Figs. 2b, c and e), which inhibits the reduction of Ru sites on the catalyst surface, resulting in fewer Ru⁰ sites on the catalyst surface (Fig. 4a) [12c]. There are still strong CO adsorption signals at NTO and Ruⁿ⁺ sites on the surfaces of these

catalysts (Ru@NTO, Ru@NTO-N and Ru@NTO-NH). Therefore, the NTO-derived overlayer will not inhibit CO adsorption.

The oxygen vacancy can enhance the CO adsorption on NTO (2173 cm⁻¹) [26], which not only related to the oxygen vacancy, but also to the specific surface area, morphology, surface charge and other factors. Thus, it is unable to determine the number of oxygen vacancies in these catalysts based on CO-adsorption FT-IR results. The electron paramagnetic resonance (EPR) was also performed to confirm oxygen vacancy and the SMSI strength (Fig. 3d). The EPR signal of Ru@NTO-NH is stronger than that of Ru@NTO-H, indicating that there are more oxygen vacancies and Ti³⁺ species on the surface of catalysts, suggesting Ru@NTO-NH contains more notable SMSI [27].

The chemical composition of the surface and the states of Ti, Na, Ru over the Ru/TiO₂ and Ru@NTO-NH were studied by XPS (Figs. 4a and b). In comparison with Ru/TiO₂, the Ru 3d_{5/2} peak of Ru@NTO-NH shifted to a higher binding energy, indicating that Ru@NTO-NH has more electron-deficient Ru NPs than Ru/TiO₂ since the NaTiO_x overlayer may inhibit the reduction of Ru NPs [20]. The peaks of Na 1 s and Ti 2p move higher binding energy after the loading of Ru, suggesting that there was electron transfer from NTO to Ru NPs (Figs. 4b and c) [15a]. The signal peaks of Ti 2p and Na 1 s shift towards lower binding energy in the order of Ru@NTO-H, Ru@NTO, and Ru@NTO-NH, indicating that the doping of alkali metals and more incompletely coordinated Ti³⁺ cations and oxygen vacancies on the Ru@NTO-NH catalyst [15a,28]. Among them, the Ti 2p_{3/2} peak deconvolutes to two peaks at around 458.6 and 458.1 eV, corresponding to Ti⁴⁺ and Ti³⁺, respectively. The ratio of the Ti³⁺ peak increases gradually in the aforementioned order (Table S3). The binding energy order of Ru 3d signal is opposite to Na 1 s. Ru exists in the mixed states of metal state (Ru⁰) and positively charged state (Ruⁿ⁺). The ratio of Ruⁿ⁺/Ru⁰ is 1.59 (Ru@NTO-NH), 1.13 (Ru@NTO) and 0.75 (Ru@NTO-H), respectively (Fig. 4a and Table S4), indicating that Ru@NTO-NH are more electron deficient.

In accordance with the above results, the formation mechanism of different NTO supported Ru catalysts was illustrated in Fig. 5. A small amount of free TiO₃²⁻ will be adsorbed on the surface of Ru NPs during the impregnation reduction process. NaTiO_x-coating is different with TiO_x-coating, because it will be weakened under H₂ calcination conditions [15a]. The N₂ calcination enhances the crystallinity of the catalyst [29], which can avoid the incomplete overlayer caused by over-excessive reduction of NaTiO_x coating in the H₂ reduction process. H₂ reduction can make the dispersion of Ru species more evenly in the support and weaken the NaTiO_x coating of Ru NPs.

To further elucidate the role of the unique SMSI overlayers over the interface of Ru@NTO-NH, we performed hydrogen temperature programmed desorption (H₂-TPD) experiments on Ru/TiO₂ and Ru@NTO-NH (Fig. 6a, Table S5). The desorption peak at 89 °C of Ru@NTO-NH and 151 °C of Ru/TiO₂ can be attributed to the H₂ desorption on the

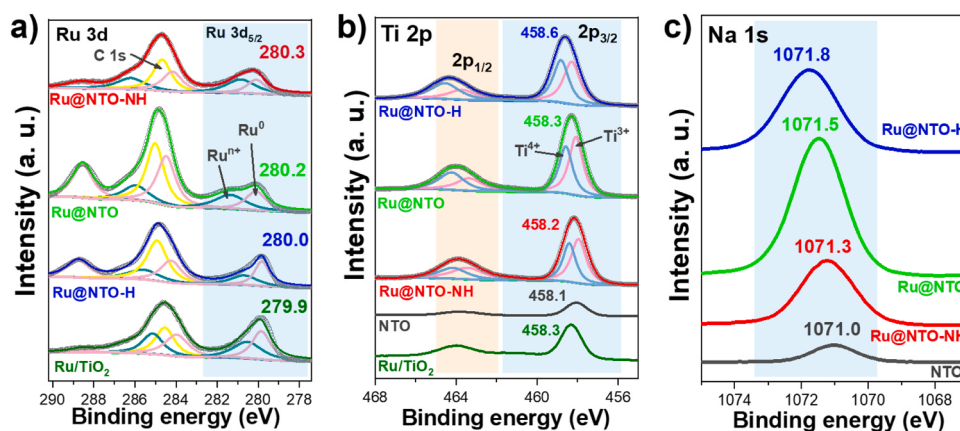


Fig. 4. (a) Ru 3d (b) Ti 2p and (c) Na 1 s XPS spectra of NTO, Ru@NTO, Ru@NTO-H, Ru/TiO₂ and Ru@NTO-NH. The Ru loading of the above materials is 5 wt%.

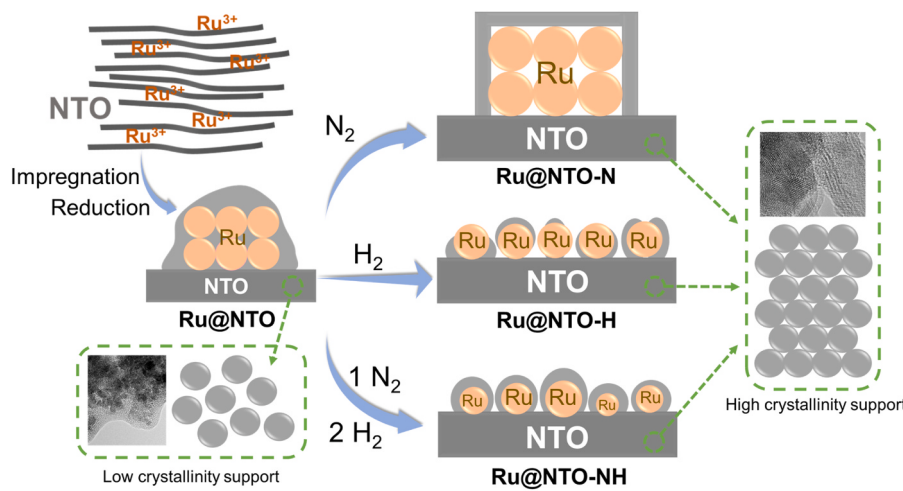


Fig. 5. The formation mechanism of different NTO supported Ru catalysts.

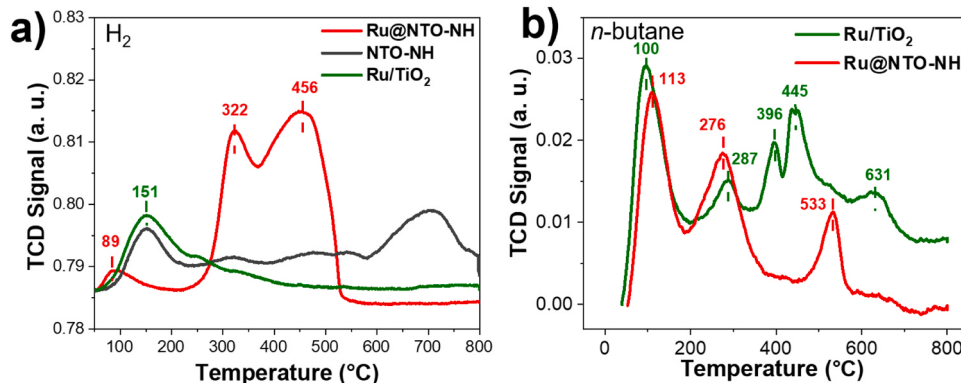


Fig. 6. (a) H_2 -TPD and (b) n -butane-TPD profiles of Ru/TiO_2 and $Ru@NTO-NH$.

Ru adsorption site [30]. The large desorption peaks of $Ru@NTO-NH$ at high temperatures (322 °C and 456 °C) are correlated to the reverse hydrogen spillover from NTO to Ru [15a,31]. It is worth noting that there are obvious H_2 desorption peaks in the H_2 -TPD of NTO-NH, indicating that H_2 can be adsorbed on the NTO. Therefore, $Ru@NTO-NH$ has better H_2 activation ability and higher H^* coverage than Ru/TiO_2 . Butane-TPD tests were performed to investigate the affinities of the Ru/TiO_2 and $Ru@NTO-NH$ to alkanes (Fig. 6b, Table S6). Compared with Ru/TiO_2 , $Ru@NTO-NH$ has higher butane desorption rate and

amount, suggesting that the $NaTiO_x$ overlayers weakens the interactions between Ru NPs and alkyl chains, facilitating the desorption of alkyl chains.

The catalytic activity of different metal oxides supported Ru catalysts were investigated for LDPE hydrogenolysis reaction (Fig. 7a, Table S7). The catalytic activity for LDPE hydrogenolysis follows the order of $Ru/TiO_2 > Ru/\gamma-Al_2O_3 > Ru/CeO_2 > Ru/MgO > Ru/WO_3$. The LDPE hydrogenolysis activity over Ru/TiO_2 catalyst reaches 79%, but liquid alkane selectivity is poor (46%). The catalytic performance of NTO

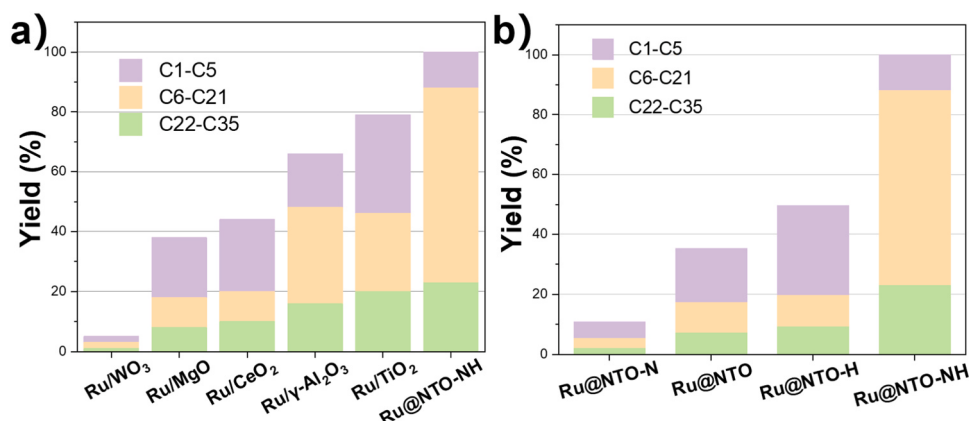


Fig. 7. (a) Yield distribution of LDPE hydrogenolysis over different supported Ru catalysts. (b) Yield distribution of LDPE hydrogenolysis catalyzed by NTO supported Ru catalysts. Reaction conditions: LDPE (500 mg), 5 wt% Ru Cat. (100 mg), 180 °C, 8 h, 1 MPa H_2 .

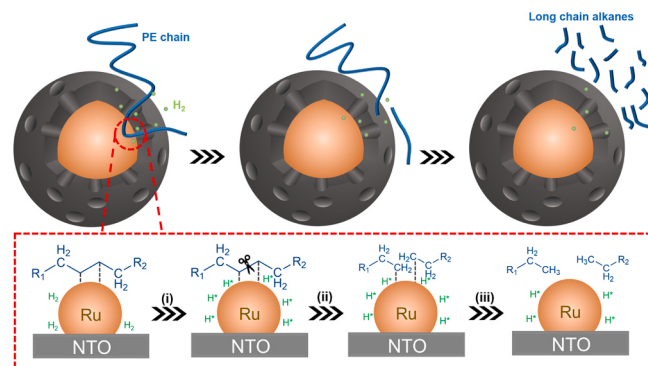
supported Ru catalysts on the LDPE hydrogenolysis was also studied (Fig. 7b, Table S8, entries 1–4). The catalytic activity for LDPE hydrogenolysis is in the order of Ru@NTO-NH > Ru@NTO-H > Ru@NTO > Ru@NTO-N. Ru@NTO-NH exhibits excellent LDPE hydrogenolysis activity and liquid alkane selectivity. The distribution of liquid products was analyzed by GC-MS (Fig. S7). Obvious aggregation of Ru NPs is observed in the cases of Ru@NTO and Ru@NTO-N, so both of them exhibits poor catalytic activity on the LDPE hydrogenolysis. In comparison of Ru@NTO-NH, Ru@NTO-H contains more electron-rich Ru NPs whose have incomplete NaTiO_x-overlayer, so it exhibits poor catalytic activity and liquid alkane selectivity for LDPE hydrogenolysis.

In view of N₂ possible activation effects on Ru, Ru@NTO-ArH prepared by calcination under Ar is used for the hydrogenolysis of LDPE. The experimental results are roughly consistent with Ru@NTO-NH (Table S8, entry 5). The catalytic efficiency of Ru/HTO-NH is significant decrease, with only 31% conversion obtained under the same conditions (Table S8, entry 6). Therefore, the presence of Na⁺ can effectively improve the performance of the catalyst, since Na⁺ can also provide more base sites of catalysts, which is beneficial for the uniform dispersion of Ru species [17]. The conversion of Ru/NTO-NH hydrogenolysis LDPE decreased to 5% (Table S8, entry 7), so that the NaBH₄ reduction step is crucial to improve the catalytic activity of the catalyst.

According to structural characterization data, the excellent performance of Ru@NTO-NH can be attributed to prominent SMSI between Ru and NTO, thereby leading to smaller, more positively charged Ru NP coated by NaTiO_x. Ru@NTO-NH contains smaller and more positively charged Ru NPs than other Ru catalysts (Ru/TiO₂, Ru@NTO, Ru@NTO-N and Ru@NTO-H) (detected by TEM and XPS) (Fig. 2 and Fig. 4), which is conducive to H₂ activation and H* coverage (confirmed by H₂-TPD), thereby improving the catalytic activity and selectivity [10a,12b]. Furthermore, the NaTiO_x overlayer on Ru NPs does not affect the activation of H₂ (small molecule gas can enter freely based on CO adsorption

and H₂-TPD experiments), but weakens the adsorption ability for LDPE (verified by butane-TPD) [3,12b]. The mechanism for hydrogenolysis of alkane C-C follows dehydrogenation and hydrocracking routes, so the deceased absorbability for LDPE is advantageous to the cleavage of its internal C-C bonds [9a,9c,10a,32].

The effects of Ru loading, reaction temperature, reaction time, and H₂ pressure on the conversion and selectivity are also investigated (Fig. 8). The conversion and liquid phase selectivity of Ru-supported NTO catalysts increase with Ru loading (Fig. 8a, Table S9). Higher (200 °C) reaction temperature did not improve the selectivity of the liquid products, and low temperature (< 180 °C) had poor conversion and liquid product selectivity (Fig. 8b, Table S10). LDPE can be completely converted after 8 h (Fig. 8c), and further prolonging the reaction time would reduce the reaction selectivity for high-value long-chain alkanes (Table S11). In the case of Ru@NTO-NH, the best



Scheme 1. Hydrogen hydrolysis of polyolefin long chain on Ru@NTO-NH.

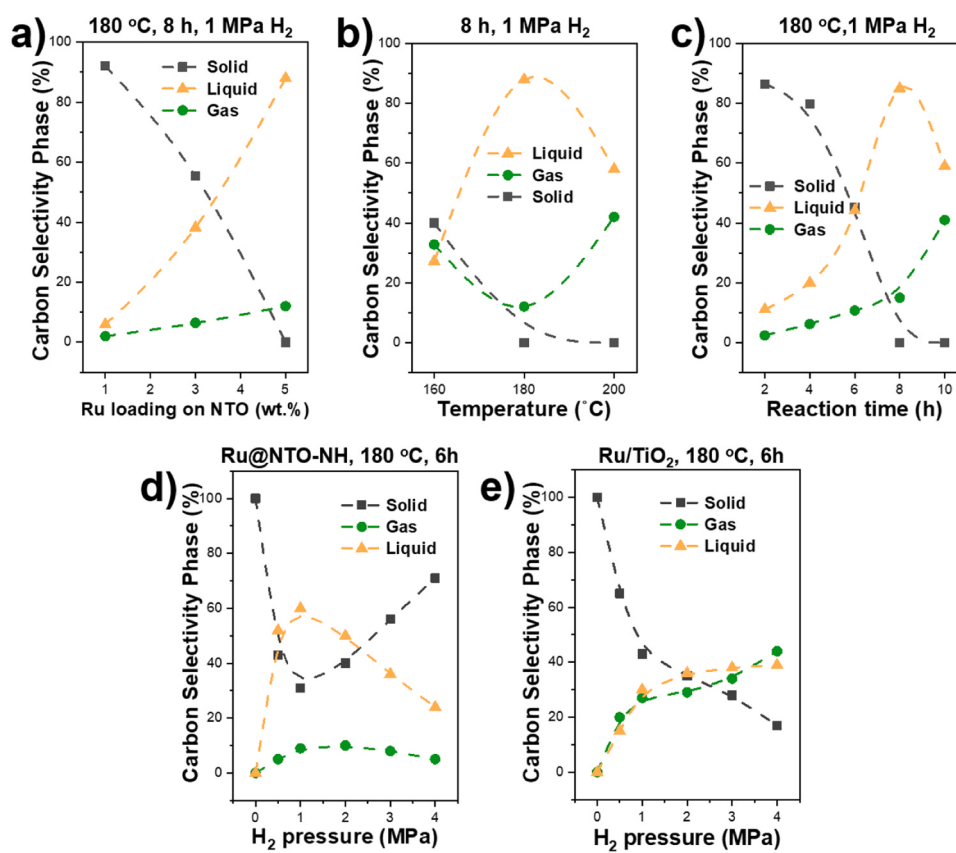


Fig. 8. The effects of (a) Ru loading, (b) reaction temperature, (c) reaction time, (d) H₂ pressure on the Ru@NTO-NH catalyzed LDPE hydrogenolysis. (e) The effects of H₂ pressure on the Ru/TiO₂ catalyzed LDPE hydrogenolysis. Reaction condition: LDPE (500 mg), Ru catalyst (100 mg, 5 wt% of Ru).

conversion and the liquid alkanes selectivity is observed under 1 MPa H₂ (Fig. 8d, Table S12). In contrast, the hydrogenolysis conversion of LDPE increases monotonously with hydrogen pressure in the same range of 0.5–4.0 MPa H₂ over Ru/TiO₂ (Fig. 8e, Table S13). The H₂ chemisorption equilibrium constant was calculated by the Langmuir equation. The H₂ chemisorption equilibrium constant of Ru@NTO-NH is about twice of Ru/TiO₂ at 50 °C (Fig. S8), demonstrating that the *H binding energy on Ru@NTO-NH is stronger than Ru/TiO₂ under the same hydrogen pressure [10a]. The negative rate dependence on H₂ pressure on Ru@NTO-NH is attributed to its higher active H* coverage than Ru/TiO₂ and the competitive adsorption of active H* and alkyl chains [33].

According to the experimental, characterization and literature results [8,10,12a], the mechanism of PE hydrogenolysis on Ru@NTO-NH is illustrated in Scheme 1. (1) Although there are NaTiO_x coatings on the surface of Ru NPs in the catalyst, it does not affect the adsorption of H₂ and PE chains, which is confirmed by H₂- and n-butane-TPD results. Therefore, it is likely that the PE chains and H₂ are adsorbed and activated on the Ru NPs surface through the pore structure of the NaTiO_x overlayer [8]. (2) The C-C bonds break into two alkyls adsorbed on the Ru sites under the synergistic action of the Ru catalytic center and H*. The enhanced SMSI between Ru and NTO facilitates the formation of smaller, more positively charged Ru NPs, which enhances the H* coverage on the catalyst surface, thereby promoting the internal C-C

bond cleavage step [10a]. (3) Alkane products are yielded by the alkyl hydrogenation process, following by alkane desorption from Ru NPs. The NaTiO_x-coated Ru NPs weakens the adsorption ability of alkane molecules, which accelerates the alkane desorption steps, thus improving the selectivity of long alkane products [12b].

In order to further demonstrate the potential of Ru@NTO-NH, the scale-up LDPE hydrogenolysis (2 g) was performed (Fig. 9a). At 180 °C, LDPE could be completely converted within 24 h with a liquid selectivity of 91%. In addition, LDPE could be completely converted within 4 h at higher temperature (240 °C) and H₂ pressure (4 MPa) with 90% selectivity of liquid fuel, which is better than most of previously reported Ru-based catalysts for LDPE hydrogenolysis (Fig. S9) [9a,10a, 10b,11,12a].

Encouraged by the remarkable results, Ru@NTO-NH was applied in the hydrogenolysis of other polyolefins, including LDPE plastic bags, HDPE, and PP (Fig. 9b, Table S14). The conversion rate of LDPE plastic bags reaches 93%. After increasing the temperature to 200 °C, the hydrogenolysis conversion of HDPE reaches 90%, and satisfactory selectivity for liquid fuel and wax is observed. The conversion of PP at 200 °C for 16 h is only 70% under identical conditions, but the selectivity for liquid fuel and wax is still good (77%). In order to simulate the hydrogenolysis of mixed plastics that actually exists in waste plastic treatment, gram-scale hydrogenolysis of commercial mixed waste polyolefin plastics is also carried out, which displays similar reactivity to

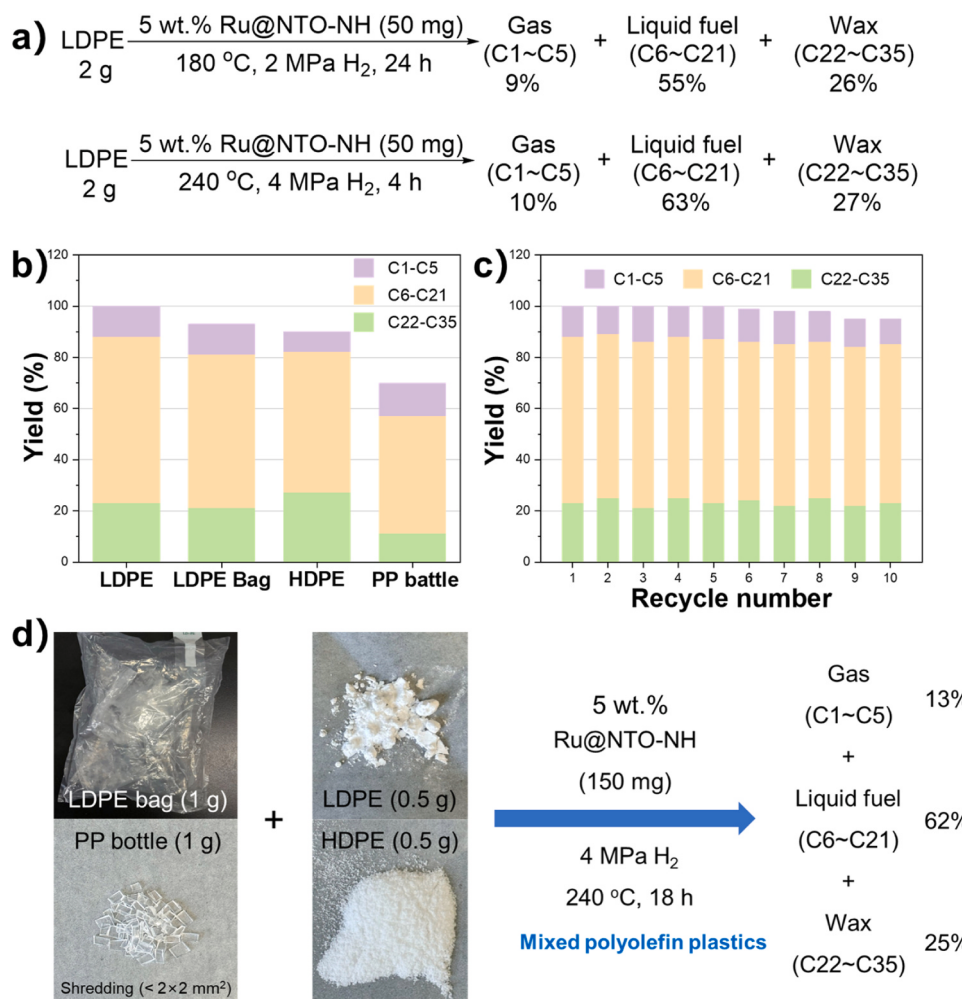


Fig. 9. (a) The scale-up LDPE hydrogenolysis. (b) Hydrogenolysis of LDPE, LDPE plastic bags, HDPE and PP with Ru@NTO-NH catalyst. Reaction condition: polyolefin (500 mg), 5 wt% Ru@NTO-NH (100 mg), 1 MPa H₂, LDPE (180 °C, 8 h), LDPE bag (180 °C, 8 h), HDPE (200 °C, 8 h), PP (200 °C, 16 h). (c) Recyclability of Ru@NTO-NH. Reaction conditions: LDPE (500 mg), 5 wt% Ru@NTO-NH (100 mg), 180 °C, 8 h. (d) Hydrogenolysis of mixed polyolefin plastics with Ru@NTO-NH catalyst.

LDPE hydrogenolysis in a slightly longer reaction time (18 h), and the yield of liquid fuel and wax was 87% (Fig. 9d).

Finally, the recyclability of Ru@NTO-NH by hydrogenolysis of LDPE was investigated. After the reaction was completed, Ru@NTO-NH was filtered and washed, and directly reused for the next reaction cycle. As shown in Fig. 8b, only a minor loss in yield was observed after 10 runs, even there is a certain amount of catalyst loss (1–2 wt% each cycle) (Fig. 9c, Table S15). Furthermore, the used catalyst has been respectively characterized by XRD, TEM, HRTEM, XPS and ICP techniques to reveal the physical properties and the chemical environment at the catalyst interface. No Ru signal is observed in the XRD diagram of the used catalyst, which rule out the agglomeration of Ru particles during use (Fig. S5). TEM and HRTEM images show the NaTiO_x overlayer still exists, but more severe aggregation and fracture of NaTiO_x nanowires are observed (Fig. S10).

After 10 runs, there is almost no loss of ruthenium metal based on ICP results (Table S1). For the recycled catalyst, the peaks of Na 1 s and Ti 2p moved to high binding energies and the Ru 3d_{5/2} peak shifted slightly to low binding energy owing to high temperature reduction reaction conditions. (Fig. S11). Furthermore, the residual low-molecular-weight polyolefins deposited on the Ru@NTO-NH catalyst after multiple catalytic cycles were investigated by O₂-TPO. Compared with fresh Ru@NTO-NH, CO₂ was detected at different temperatures in the O₂-TPO effluent of the catalyst recycled 10 times (Fig. S12). Therefore, electron transfer and carbon deposition may be responsible for the slight decrease in catalyst activity.

4. Conclusions

In summary, this novel Ru@NTO-NH catalyst exhibits excellent activity for polyolefin hydrogenolysis due to the SMSI between Ru and NTO. Several characterizations and comparative experiments have been conducted, indicating that the NaTiO_x overlayer derived from NTO effectively encapsulates the Ru nanoparticles (NPs) without impeding the adsorption of small gas molecules. Furthermore, the enhanced SMSI between Ru and NTO facilitates the formation of smaller, more positively charged and NaTiO_x-coated Ru NPs. This structural feature enhances the H⁺ coverage on the catalyst surface and weakens the adsorption ability of alkane molecules, thereby leading to excellent catalytic performance in polyolefin hydrogenolysis with high selectivity. The Ru@NTO-NH catalyst also exhibits impressive conversion and selectivity towards long-chain alkanes in the hydrogenolysis of HDPE, PP, and real LDPE plastic bags. Additionally, it demonstrates excellent stability and recyclability, as evidenced by negligible activity degradation even after 10 reaction cycles. This novel conformational relationship between catalyst structure and function exposes exciting opportunities to engineer plastic recycling and upcycling.

CRediT authorship contribution statement

Xueping Zhang: Conceptualization, Methodology, Validation, Formal analysis, Investigation, Data curation, Writing – original draft, Writing – review & editing. **Quan Gan:** Investigation, Data curation. **Peng Zhou:** Writing – review & editing. **Zhong Chen:** Writing – review & editing. **Zehui Zhang:** Writing – review & editing. **Guo-Ping Lu:** Conceptualization, Formal analysis, Writing – review & editing, Supervision, Funding acquisition.

Declaration of Competing Interest

There are no conflicts to declare.

Data availability

No data was used for the research described in the article.

Appendix A. Supporting information

Supplementary data associated with this article can be found in the online version at doi:10.1016/j.apcatb.2023.123626.

References

- [1] (a) G. Roland, J.R. Jambeck, K.L. Law, Production, use, and fate of all plastics ever made, *Sci. Adv.* 3 (2017), e1700782;
(b) K. Lee, Y. Jing, Y. Wang, N. Yan, A unified view on catalytic conversion of biomass and waste plastics, *Nat. Rev. Chem.* 6 (2022) 635–652.
- [2] C. Wang, H. Han, Y. Wu, D. Astruc, Nanocatalyzed upcycling of the plastic wastes for a circular economy, *Coord. Chem. Rev.* 458 (2022), 214422.
- [3] G. Celik, R.M. Kennedy, R.A. Hackler, M. Ferrandon, A. Tennakoon, S. Patnaik, A. M. LaPointe, S.C. Ammal, A. Heyden, F.A. Perras, M. Pruski, S.L. Scott, K. R. Poepelmeier, A.D. Sadow, M. Delferro, Upcycling single-use polyethylene into high-quality liquid products, *ACS Cent. Sci.* 5 (2019) 1795–1803.
- [4] (a) A. Rahimi, J.M. García, Chemical recycling of waste plastics for new materials production, *Nat. Rev. Chem.* 1 (2017) 0046;
(b) L.D. Ellis, N.A. Rorrer, K.P. Sullivan, M. Otto, J.E. McGeehan, Y. Román-Leshkov, N. Wierckx, G.T. Beckham, Chemical and biological catalysts for plastics recycling and upcycling, *Nat. Catal.* 4 (2021) 539–556.
- [5] (a) S.M. Al-Salem, P. Lettieri, J. Baeyens, Recycling and recovery routes of plastic solid waste (PSW): a review, *Waste Manag.* 29 (2009) 2625–2643;
(b) A.S. Goldman, Catalytic alkane metathesis by tandem alkane dehydrogenation–olefin metathesis, *Science* 312 (2006) 257–261;
(c) L.D. Ellis, S.V. Orski, G.A. Kenlaw, A.G. Norman, K.L. Beers, Y. Román-Leshkov, G.T. Beckham, Tandem heterogeneous catalysis for polyethylene depolymerization via an olefin-intermediate process, *ACS Sustain. Chem. Eng.* 9 (2021) 623–628;
(d) L.O. Mark, M.C. Cendejas, I. Hermans, The use of heterogeneous catalysis in the chemical valorization of plastic waste, *ChemSusChem* 13 (2020) 5808–5836;
(e) D.P. Serrano, J. Aguado, J.M. Escola, Developing advanced catalysts for the conversion of polyolefinic waste plastics into fuels and chemicals, *ACS Catal.* 2 (2012) 1924–1941.
- [6] (a) F. Zhang, M. Zeng, R.D. Yappert, J. Sun, Y.H. Lee, A.M. LaPointe, B. Peters, M. M. Abu-Omar, S.L. Scott, Polyethylene upcycling to long-chain alkylaromatics by tandem hydrogenolysis/aromatization, *Science* 370 (2020) 437–441;
(b) X. Wu, A. Tennakoon, R. Yappert, M. Esveld, M.S. Ferrandon, R.A. Hackler, A. M. LaPointe, A. Heyden, M. Delferro, B. Peters, A.D. Sadow, W.Y. Huang, Size-controlled nanoparticles embedded in a mesoporous architecture leading to efficient and selective hydrogenolysis of polyolefins, *J. Am. Chem. Soc.* 144 (2022) 5323–5334.
- [7] (a) S.D.A. Sharuddin, F. Abnisa, W.M.A.W. Daud, M.K. Aroua, A review on pyrolysis of plastic wastes, *Energy Convers. Manag.* 115 (2016) 308–326.(b) Miandad, R.; Barakat, M.A.; Aburazaiqa, A.S.; Rehan, M.; Nizami, A.S. Catalytic pyrolysis of plastic waste: a review *Process Saf. Environ. Prot.* 102 (2016) 822 838.
- [8] A. Tennakoon, X. Wu, A.L. Paterson, S. Patnaik, Y.C. Pei, A.M. LaPointe, S. C. Ammal, R.A. Hackler, A. Heyden, I.I. Slowing, G.W. Coates, M. Delferro, B. Peters, W.Y. Huang, A.D. Sadow, F.A. Perras, Catalytic upcycling of high-density polyethylene via a processive mechanism, *Nat. Catal.* 3 (2020) 893–901.
- [9] (a) L. Chen, Y. Zhu, L.C. Meyer, L.V. Hale, T.T. Le, A. Karkamkar, J.A. Lercher, O. Y. Gutiérrez, J. Szanyi, Effect of reaction conditions on the hydrogenolysis of polypropylene and polyethylene into gas and liquid alkanes, *React. Chem. Eng.* 7 (2022) 844–854;
(b) J.E. Rorrer, C. royan-Valls, G.T. Beckham, Y. Román-Leshkov, Hydrogenolysis of polypropylene and mixed polyolefin plastic waste over Ru/C to produce liquid alkanes, *ACS Sustain. Chem. Eng.* 9 (2021) 11661–11666;
(c) C.H. Jia, S.Q. Xie, W.L. Zhang, N.N. Intan, J. Sampath, J. Pfandtner, H.F. Lin, Deconstruction of high-density polyethylene into liquid hydrocarbon fuels and lubricants by hydrogenolysis over Ru catalyst, *Chem. Catal.* 1 (2021) 437–455;
(d) J.E. Rorrer, G.T. Beckham, Y. Román-Leshkov, Conversion of polyolefin waste to liquid alkanes with Ru-based catalysts under mild conditions, *JACS Au* 1 (2021) 8–12.
- [10] (a) L.X. Chen, L.C. Meyer, L. Kovarik, D. Meira, X.I. Pereira-Hernandez, H.H. Shi, K. Khivantsev, O.Y. Gutiérrez, J. Szanyi, Disordered, sub-nanometer Ru structures on CeO₂ are highly efficient and selective catalysts in polymer upcycling by hydrogenolysis, *ACS Catal.* 12 (2022) 4618–4627;
(b) Y. Nakaji, M. Tamura, S. Miyaoka, S. Kumagai, M. Tanji, Y. Nakagawa, T. Yoshioka, K. Tomishige, Low-temperature catalytic upgrading of waste polyolefinic plastics into liquid fuels and waxes, *Appl. Catal. B* 285 (2021), 119805.
- [11] (a) C. Wang, T.J. Xie, P.A. Kots, B.C. Vance, K.W. Yu, P. Kumar, J.Y. Fu, S.B. Liu, G. Tsilomelekis, E.A. Stach, W.Q. Zheng, D.G. Vlachos, Polyethylene hydrogenolysis at mild conditions over ruthenium on tungstated zirconia, *JACS Au* 1 (2021) 1422–1434;
(b) M. Tamura, S. Miyaoka, Y. Nakaji, M. Tanji, S. Kumagai, Y. Nakagawa, T. Yoshioka, K. Tomishige, Structure-activity relationship in hydrogenolysis of polyolefins over Ru/ support catalysts, *Appl. Catal. B* 318 (2022), 121870.
- [12] (a) P.A. Kots, S.B. Liu, B.C. Vance, C. Wang, J.D. Sheehan, D.G. Vlachos, Polypropylene plastic waste conversion to lubricants over Ru/TiO₂ catalysts, *ACS Catal.* 11 (2021) 8104–8115;
(b) P.A. Kots, T.J. Xie, B.C. Vance, C.M. Quinn, M. Dorneles de Mello, J. A. Boscoboinik, C. Wang, P. Kumar, E.A. Stach, N.S. Marinkovic, L. Ma, S.

- N. Ehrlich, D.G. Vlachos, Electronic modulation of metal-support interactions improves polypropylene hydrogenolysis over ruthenium catalysts, *Nat. Commun.* 13 (2022) 5186;
- (c) T. Kim, H. Nguyen-Phu, T. Kwon, K.H. Kang, I. Ro, Investigating the impact of TiO₂ crystalline phases on catalytic properties of Ru/TiO₂ for hydrogenolysis of polyethylene plastic waste, *Environ. Pollut.* 331 (2023), 121876;
- (d) S.D. Jaydev, M.E. Usteri, A.J. Martín, J. Pérez-Ramírez, Identifying selective catalysts in polypropylene hydrogenolysis by decoupling scission pathways, *Chem. Catal.* 3 (2023), 100564.
- [13] Y. Nakajia, Y. Nakagawaab, M. Tamuraab, K. Tomishige, Regioselective hydrogenolysis of alga-derived squalane over silica-supported ruthenium–vanadium catalyst, *Fuel Process. Technol.* 176 (2018) 249–257.
- [14] (a) S.J. Tauster, S.C. Fung, R.L. Garten, Strong metal–support interactions: occurrence among the binary oxides of groups IIA–VB, *J. Am. Chem. Soc.* 100 (1978) 170–175;
- (b) S.J. Tauster, S.C. Fung, Strong metal–support interactions: occurrence among the binary oxides of groups IIA–VB, *J. Catal.* 55 (1978) 29–35;
- (c) Z.X. Luo, G.Q. Zhao, H.G. Pan, W.P. Sun, Strong metal–support interaction in heterogeneous catalysts, *Adv. Energy Mater.* 12 (2022) 2201395;
- (d) T.C. Pu, W.H. Zhang, M.H. Zhu, Engineering heterogeneous catalysis with strong metal–support interactions: characterization, theory and manipulation, *Angew. Chem. Int. Ed.* 62 (2023), e202212278.
- [15] (a) Q.J. Pei, T. He, Y. Yu, Z.J. Jing, J.P. Guo, L. Liu, Z.T. Xiong, P. Chen, Liberating active metals from reducible oxide encapsulation for superior hydrogenation catalysis, *ACS Appl. Mater. Inter.* 12 (2020) 7071–7080;
- (b) A. Beck, X. Huang, L. Artigilia, M. Zabilskiy, X. Wang, P. Rzepka1, D. Palagin, M.G. Willinger, J. A. van Bokhoven, The dynamics of overlayer formation on catalyst nanoparticles and strong metal–support interaction, *Nat. Commun.* 11 (2020) 3220;
- (c) R.J. Huang, O. Kwon, C. Lin, R.J. Gorte, The effects of SMSI on m-Cresol hydrodeoxygenation over Pt/Nb₂O₅ and Pt/TiO₂, *J. Catal.* 398 (2021) 102–108.
- [16] (a) Y.X. Tang, Y.Y. Zhang, J.Y. Deng, J.Q. Wei, H.L. Tam, B.K. Chandran, Z. L. Dong, Z. Chen, X.D. Chen, Mechanical force-driven growth of elongated bending TiO₂-based nanotubular materials for ultrafast rechargeable lithium-ion batteries, *Adv. Mater.* 26 (2014) 6111–6118;
- (b) Y.Y. Zhan, Z.L. Jiang, J.Y. Huang, L.Y. Lim, W.L. Li, J.Y. Deng, D.G. Gong, Y. X. Tang, Y.K. Lai, Z. Chen, Titanate and titania nanostructured materials for environmental and energy applications: a review, *RSC Adv.* 5 (2015) 79479–79510.
- [17] (a) T. Song, P.Y. Zhang, T.T. Wang, A. Ali, H.P. Zeng, Alkali-assisted fabrication of holey carbon nitride nanosheet with tunable conjugated system for efficient visible-light-driven water splitting, *Appl. Catal. B* 224 (2018) 877–885;
- (b) Z.D. Huang, K. Zhang, T.T. Zhang, X.S. Yang, R.Q. Liu, Y. Li, X.J. Liu, X. M. Feng, Y.W. Ma, W. Huang, Hierarchical NiCo₂O₄ mesoporous microspheres as anode for lithium ion batteries with superior rate capability, *Energy Stor. Mater.* 3 (2016) 36–44;
- (c) J. Gao, Y. Cao, G. Luo, J.J. Fan, J.H. Clark, S.C. Zhang, High-efficiency catalytic hydrodeoxygenation of lignin-derived vanillin with nickel-supported metal phosphate catalysts, *Chem. Eng. J.* 448 (2022), 137723.
- [18] X.P. Zhang, G.P. Lu, K. Wang, Y.M. Lin, P.C. Wang, W.B. Yi, Lignin-derived Zn single atom/N-codoped porous carbon for α -alkylation of aromatic ketones with alcohols via borrowing hydrogen strategy, *Nano Res.* 15 (2022) 1874. -188.
- [19] (a) Z. Zhou, J.J. Li, Z.X. You, A facile TiO₂ containing oxygen vacancies and hydroxyl as a Ru-loaded underlay for CO₂ hydrogenation to CH₄, *Appl. Surf. Sci.* 587 (2022), 152856;
- (b) J. Wojciechowska, E. Gitzhofer, J. Grams, A.M. Ruppert, N. Keller, Light-driven synthesis of sub-nanometric metallic Ru catalysts on TiO₂, *Catal. Today* 326 (2019) 8–14.
- [20] (a) Y. Zhang, W.J. Yan, H.F. Qi, X. Su, Y. Su, X.Y. Liu, L. Li, X.F. Yang, Y.Q. Huang, T. Zhang, Strong metal–support interaction of Ru on TiO₂ derived from the co-reduction mechanism of Ru_xTi_{1-x}O₂ interphase, *ACS Catal.* 12 (2022) 1697–1705;
- (b) C. Dong, H. Wang, Y.W. Ren, Z.P. Qu, Layer MnO₂ with oxygen vacancy for improved toluene oxidation activity, *Surf. Interfaces* 22 (2021), 100897.
- [21] (a) A. Parastaev, V. Muravev, E.O. Huertas, F. van Hoof, A.J. Kimpel, T.F. Kosinov, N. Hensen, E.J.M. Boosting CO₂ hydrogenation via size-dependent metal–support interactions in cobalt/ceria-based catalysts, *Nat. Catal.* 3 (2020) 526–533;
- (b) S.D. Sun, X.M. Wu, Z.W. Huang, H.Z. Shen, H.W. Zhao, G.H. Jing, Engineering stable Pt nanoclusters on defective two-dimensional TiO₂ nanosheets by introducing SMSI for efficient ambient formaldehyde oxidation, *Chem. Eng. J.* 435 (2022), 135035;
- (c) F. Bertella, P. Concepción, A. Martínez, TiO₂ polymorph dependent SMSI effect in Co–Ru/TiO₂ catalysts and its relevance to Fischer-Tropsch synthesis, *Catal. Today* 289 (2017) 181–191;
- (d) M. Li, H. Amari, A.C. Veen, Metal–oxide interaction enhanced CO₂ activation in methanation over ceria supported nickel nanocrystallites, *Appl. Catal. B Environ.* 239 (2018) 27–35.
- [22] (a) M.Y. Zhang, X.L. Duan, Y. Gao, S.S. Zhang, X.Y. Lu, K.L. Luo, J. Ye, X.P. Wang, Q. Niu, P.F. Zhang, S. Dai, Tuning oxygen vacancies in oxides by configurational entropy, *ACS Appl. Mater. Interfaces* 15 (2023) 45774–45789;
- (b) C. Dong, H. Wang, Y.W. Ren, Z.P. Qu, Layer MnO₂ with oxygen vacancy for improved toluene oxidation activity, *Surf. Interfaces* 22 (2021), 100897.
- [23] (a) Q. Zhang, T.Q. Zhang, Y.Q. Wei, T.Y. Zhai, H.Q. Li, Removing structural water from sodium titanate anodes towards barrier-free ion diffusion for sodium ion batteries, *J. Mater. Chem. A* 5 (2017) 18691–18697;
- (b) M. Shirpour, J. Cabana, M. Doeff, New materials based on a layered sodium titanate for dual electrochemical Na and Li intercalation systems, *Energy Environ. Sci.* 6 (2013) 2538;
- (c) D.V. Bavykin, J.M. Friedrich, F.C. Walsh, Protonated titanates and TiO₂ nanostructured materials: synthesis, properties, and applications, *Adv. Mater.* 18 (2006) 2807–2824;
- (d) L.F. Que, F.D. Yu, L.L. Zheng, Z.B. Wang, D.M. Gu, Tuning lattice spacing in titanate nanowire arrays for enhanced sodium storage and long-term stability, *Nano Energy* 45 (2018) 337–345;
- (e) Q. Zhang, T.Q. Zhang, Q. Wei, Y. T.Y. Zhai, H.Q. Li, Removing structural water from sodium titanate anodes towards barrier-free ion diffusion for sodium ion batteries, *J. Mater. Chem. A* 5 (2017) 18691–18697.
- [24] (a) L.M. Martínez Tejada, A. Muñoz, M.A. Centeno, J.A. Odriozola, In-situ Raman spectroscopy study of Ru/TiO₂ catalyst in the selective methanation of CO, *J. Raman Spectrosc.* 47 (2016) 189–197;
- (b) M. Šćepanović, S. Aškrabić, V. Berec, A. Golubović, Z. Dolčević-Mitrović, A. Kremenvić, Z.V. Popović, Characterization of La-doped TiO₂ nanopowders by Raman spectroscopy, *Acta Phys. Pol. A* 115 (2009) 771–774.
- [25] (a) P. Panagiotaopoulos, X.E. Verykios, Mechanistic study of the selective methanation of CO over Ru/TiO₂ catalysts: effect of metal crystallite size on the nature of active surface species and reaction pathways, *J. Phys. Chem. C* 121 (2017) 5058–5068;
- (b) Y. Zhang, X.L. Yang, X.F. Yang, H.M. Duan, H.F. Qi, Y. Su, B.L. Liang, H.B. Tao, B. Liu, D. Chen, X. Su, Y.Q. Huang, T. Zhang, Tuning reactivity of Fischer-Tropsch synthesis by regulating TiO_x overlayer over Ru/TiO₂ nanocatalysts, *Nat. Commun.* 11 (2020) 3185.
- [26] M. Wang, M. Shen, X.X. Jin, J.J. Tian, Y.J. Zhou, Y.R. Shao, L.X. Zhang, Y.S. Li, J. L. Shi, Mild generation of surface oxygen vacancies on CeO₂ for improved CO₂ photoreduction activity, *Nanoscale* 12 (2020) 12374.
- [27] (a) S. Liang, X.R. Deng, G.Y. Xu, X. Xiao, M.F. Wang, X.S. Guo, P.A. Ma, Z. Y. Cheng, D. Zhang, J. Lin, A novel Pt-TiO₂ heterostructure with oxygen-deficient layer as bilaterally enhanced sonosensitizer for synergistic chemo-sonodynamic cancer therapy, *Adv. Funct. Mater.* 30 (2020) 1908598;
- (b) J. Li, Y.P. Lin, X.L. Pan, D.Y. Miao, D. Ding, Y. Cui, J.H. Dong, X.H. Bao, Enhanced CO₂ methanation activity of Ni/anatase catalyst by tuning strong metal–support interactions, *ACS Catal.* 9 (2019) 6342–6348;
- (c) W.X. Wang, X.K. Li, Y. Zhang, R. Zhang, H. Ge, J.C. Bi, M.X. Tang, Strong metal–support interactions between Ni and ZnO particles and their effect on the methanation performance of Ni/ZnO, *Catal. Sci. Technol.* 7 (2017) 4413;
- (d) X.Y. Liu, M.H. Liu, Y.C. Luo, C.Y. Mou, S.D. Lin, H.K. Cheng, J.M. Chen, J. F. Lee, T.S. Lin, Strong metal–support interactions between gold nanoparticles and ZnO nanorods in CO oxidation, *J. Am. Chem. Soc.* 134 (2012) 10251–10258.
- [28] (a) L. Zhou, S.R. He, X.H. Xu, G.W. Li, C.C. Jia, Potassium titanate supported atomically dispersed palladium for catalytic oxidation, *Adv. Sci.* (2022) 2204674;
- (b) Y.Y. Wu, C.Y. Li, B.Y. Fang, X.Y. Wang, J. Ni, B.Y. Lin, J.X. Lin, L.L. Jiang, Enhanced ammonia synthesis performance of ceria-supported Ru catalysts via introduction of titanium, *Chem. Commun.* 56 (2020) 1141–1144;
- (c) X.C. Wang, P.X. Wu, Z.Q. Wang, L.L. Zhou, Y.C. Liu, H.Y. Cheng, M. Arai, C. Zhang, F.Y. Zhao, Chlorine-modified Ru/TiO₂ catalyst for selective guaiacol hydrodeoxygenation, *ACS Sustain. Chem. Eng.* 9 (2021) 3083–3094;
- (d) M. Xu, S. He, H. Chen, G.Q. Cui, L.R. Zheng, B. Wang, M. Wei, TiO_{2-x}-modified Ni nanocatalyst with tunable metal–support interaction for water-gas shift reaction, *ACS Catal.* 7 (2017) 7600–7609.
- [29] (a) Z.W. Gao, B. Ma, S. Chen, J.Q. Tian, C. Zhao, Converting waste PET plastics into automobile fuels and antifreeze components, *Nat. Commun.* 13 (2022) 3343;
- (b) X. Hai, S.B. Xi, S. Mitchell, K. Harrath, H.M. Xu, D.F. Akl, D.B. Kong, J. Li, Z. J. Li, T. Sun, H.M. Yang, Y.G. Cui, C.L. Su, X.X. Zhao, J. Li, J. Pérez-Ramírez, J. Lu, Scalable two-step annealing method for preparing ultra-high-density single-atom catalyst libraries, *Nat. Nanotechnol.* 17 (2022) 174–181.
- [30] (a) P. Panagiotaopoulos, D.I. Kondarides, Effects of alkali additives on the physicochemical characteristics and chemisorptive properties of Pt/TiO₂ catalysts, *J. Catal.* 260 (2008) 141–149;
- (b) H.Y. Lin, Y.W. Chen, The kinetics of H₂ adsorption on supported ruthenium catalysts, *Thermochim. Acta* 419 (2004) 283–290.
- [31] (a) H. Shi, O.Y. Gutiérrez, G.L. Haller, D.H. Mei, R. Rousseau, J.A. Lercher, Structure sensitivity of hydrogenolytic cleavage of endocyclic and exocyclic C–C bonds in methylcyclohexane over supported iridium particles, *J. Catal.* 297 (2013) 70–78;
- (b) D.D. Hibbitts, D.W. Flaherty, E. Iglesia, Effects of chain length on the mechanism and rates of metal-catalyzed hydrogenolysis of n-alkanes, *J. Phys. Chem. C* 120 (2016) 8125–8138.
- [32] (a) D.W. Flaherty, E. Iglesia, Transition-state enthalpy and entropy effects on reactivity and selectivity in hydrogenolysis of n-alkanes, *J. Am. Chem. Soc.* 135 (2013) 18586–18599;
- (b) D.W. Flaherty, D.D. Hibbitts, E. Iglesia, Metal-catalyzed C–C bond cleavage in alkanes: effects of methyl substitution on transition-state structures and stability, *J. Am. Chem. Soc.* 136 (2014) 9664–9676.
- [33] P. Panagiotaopoulos, D.I. Kondarides, X.E. Verykios, Mechanistic study of the selective methanation of CO over Ru/TiO₂ catalyst: identification of active surface species and reaction pathways, *J. Phys. Chem. C* 115 (2011) 1220–1230.